THE SEISMOLOGICAL SOCIETY OF AMERICA
400 Evelyn Ave., Suite 201
Albany, CA 94706-1375
(510) 525-5474; FAX (510) 525-7204
www.seismosoc.org

Bulletin of the Seismological Society of America, Vol. 100, No. 3, pp. 1165–1173, June 2010, doi: 10.1785/0120090277

Frequency-Magnitude Characteristics Down to Magnitude −4.4 for Induced Seismicity Recorded at Mponeng Gold Mine, South Africa

by G. Kwiatek, K. Plenkers, M. Nakatani, Y. Yabe, G. Dresen, and JAGUARS-Group

Abstract This article aims to investigate the frequency-magnitude characteristics and lower magnitude limits of the microseismic catalog recorded with a seismic network sensitive to high frequencies at Mponeng mine, South Africa. The network, composed of one three-component accelerometer and eight acoustic emission sensors, is located at a depth of 3.5 km below the surface and covers the limited volume of approximately 300 × 300 × 300 m. The three-component accelerometer was used to estimate the moment magnitude for the limited number of 135 events (M_w ranged from −4.1 to −0.3) well recorded by the network. We use the relation between the moment magnitude estimated from accelerometer data and radiated energy/moment magnitude estimated from acoustic emission sensors to extend the catalog to lower magnitudes. The magnitude of completeness of selected spatiotemporal subsets of the catalog was estimated for: (1) an aftershock sequence of an M_w 1.9 event that occurred approximately 30 m from the network, and (2) postblasting activity during working days, located more than 80 m from the network. The data follow the Gutenberg–Richter (GR) frequency-magnitude relationship with no visible deviation from self-similar behavior of seismicity between M_w −4.4 and −1.9 for the aftershock sequence and between −3.5 and −1.5 for the postblasting dataset. We estimated the magnitude of completeness of selected subset as low as −4.3 ($b = 1.26$) for the aftershock sequence and −3.4 ($b = 1.17$) for the postblasting activity. Differences in magnitude of completeness are attributed to location of recorded activity and site effects.

Introduction

The study of seismic events with extremely small magnitudes bridges the gap in magnitude scale between laboratory experiments and seismic events occurring on natural faults, which is a topic of debate for some time (e.g., Brace and Byerlee; 1966; McGarr, 1999; Kanamori and Heaton, 2000; Rice and Cocco, 2007). In addition mining-induced seismicity gives insight into processes governing nucleation (Dieterich, 1992) and allows testing the concept of minimum earthquake size (e.g., Ida, 1973; Richardson and Jordan, 2002; Boettcher *et al.*, 2009).

Based on the theory of a minimum earthquake size several studies assume that the Gutenberg–Richter (GR) frequency-magnitude distribution has a lower cut-off (Aki 1987; Dieterich, 1979). Richardson and Jordan (2002) analyzed geophone data recorded in deep mines in South Africa and suggested a lower magnitude cut-off at $M_w \sim 0$. Smaller events were regarded as being generated by a different mechanism showing a change in frequency-magnitude distribution. Recent work by Boettcher *et al.* (2009) using a high-quality catalog of geophone data also recorded in South African deep mines, showed that the lower limit, if it exists, must be below $M_w - 1.3$.

In order to extend the magnitude range of natural seismicity to smaller events, we (Japanese-German Underground Acoustic Emission Research in South Africa, JAGUARS group) installed a combined network of accelerometer and piezoelectric acoustic emission (AE) sensors in Mponeng Gold Mine in South Africa (Nakatani *et al.*, 2008). The network is capable of recording events with $M_w < 0.5$ and frequencies between 700 Hz and 200 kHz.

In this article the lower magnitude limit of the JAGUARS seismic catalog is studied, and the frequency-magnitude GR distributions are analyzed. The AE sensors were calibrated using the accelerometric data and then used to estimate the magnitude of recorded seismicity. The analyzed catalog contains events below magnitude −1.0 down to events with magnitudes lower than −4.4 (source radius of a few centimeters). The resulting magnitude catalog is composed of two different subsets. The first subset is related to the M_w 1.9 event aftershock sequence that occurred close to our network (Yabe *et al.*,

2009). The second subset contains events recorded after blasting took place at the reef. Each subset contains up to a ~7000 microearthquakes. We calculate the GR distributions and determine the magnitude of completeness for selected subsets. We find that GR power law $\log_{10} N = a - bM$ is a suitable model for describing the analyzed seismicity. We discuss the observed deviations of the GR relation and find them related to the spatial distribution of recorded activity and waveform processing.

Network

JAGUARS' network (Fig. 1b) is installed in Mponeng Gold Mine, Carletonville, South Africa, and managed by AngloGold Ashanti (Nakatani *et al.*, 2008). The mine produces gold from the proterozoic Witwatersrand formation. The gold reef (Ventersdorp Contact Reef) is at the contact between the Ventersdorp lava above and the Witwatersrand quartzites below. The reef is dipping with 26.5° to the southeast with a thickness up to 0.5–1 m. JAGUARS' network is located at 3543 m depth, about 90 m below the gold reef. The location of the network was chosen close to a nearly vertically inclined dike (Pink Green dike) with about 30 m thickness, crossing reef and tunnel levels. The dike serves as a support pillar in the mining-induced excavation. In 2007 and 2008 mining activity approached the eastern part of the dike above the network, introducing significant stress changes and microseismicity in the whole area.

For the purpose of this article, a triaxial accelerometer (composed of Wilcoxon 736T sensors) was installed. This sensor has a flat frequency response between 100 Hz and 25 kHz. Additionally, eight uniaxial acoustic emission (AE) sensors and two strainmeters were installed. The piezoelectric AE sensors are sensitive in a very high-frequency range (700 Hz–200 kHz). Seven AE sensors were of bottom-view type and one sensor was of side-view type. A band-pass filter (1 kHz–180 kHz) was applied because of unstable recordings at higher and lower frequencies. The amplitude frequency characteristic of the AE sensors is reasonably flat (for the purpose of this study) in the frequency range between 1 kHz and 60 kHz with multiple resonant frequency peaks above. We expect that the frequency characteristics of AE sensors do not affect the recorded amplitudes for events with $M_w > -4.5$ and therefore are not crucial for the purpose of our study. It is assumed that the recordings from AE sensors are proportional to ground velocity, as suggested by Collins *et al.* (2002) and Manthei (2005). Both types of instruments are installed in boreholes of various depths between 6.0 and 15.0 m to avoid the excavation damage zone around the tunnel. Boreholes are drilled upward as well as downward in order to vary the depth of sensors and improve the aperture of the network.

The acquisition system developed by Gesellschaft für Materialprüfung und Geophysik (GMuG mbH) (see, e.g., Manthei, 2005) is working in a triggering mode with a sampling frequency of 500 kHz. Waveforms are stored in a time window of ~65 ms (32,768 samples). An automatic picking routine and hypocenter location procedure is performed *in situ*. *P* and *S* waves are picked automatically using a modified least-squares algorithm and an analysis of the frequency content of the signals. An event is required to be picked at a minimum of six channels to be located. Since June 2007, the network recorded more that 500,000 waveforms as described by Plenkers *et al.* (2010). The events are typically located within ~300 m around the network (Nakatani *et al.*, 2008).

Data

In this article we focus on data recorded in a period from 27 December 2007 to 3 January 2008 when a moment

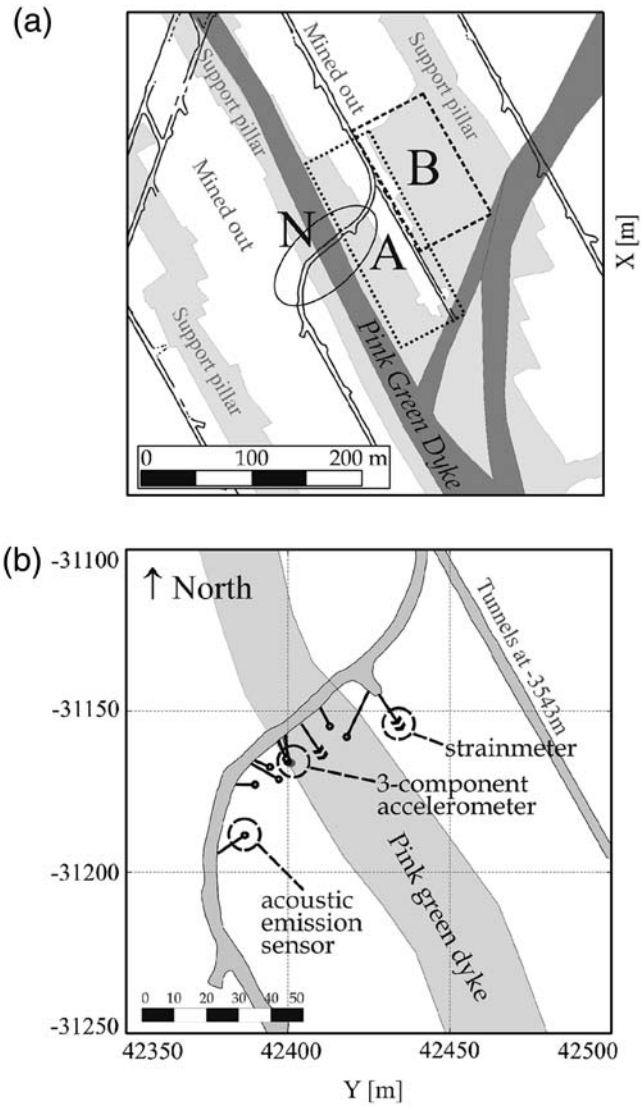

Figure 1. (a) Mining activity in the vicinity of JAGUARS' network (ellipse N). The tunnels at 3543 m depth are shown using thick black lines. The support pillars are marked light gray and the Greater Green Dike is shown in dark gray. The mined areas (A and B) are surrounded with dashed rectangles; they are located ~80 m above the monitoring site. (b) The surface distribution of the sensors used in JAGUARS' project, together with the main geological features and engineered structures in the vicinity of the network.

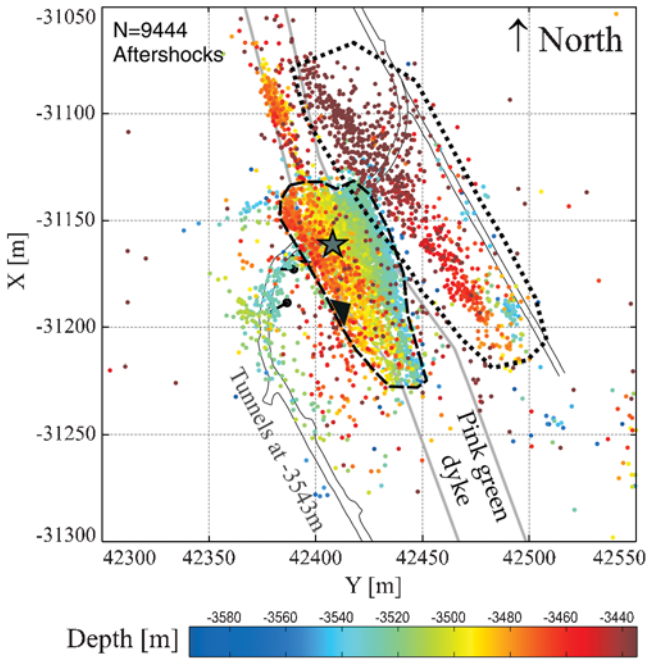

Figure 2. Spatial distribution of the aftershock sequence of the M_w 1.9 event (star) ($N = 9444$ events). The color reflects the depth of the aftershocks. The fault plane of the main rupture is shown by the dashed black line; the black triangle indicates the dip direction (northeast). The activity induced by the mainshock at the stope level (west and above the fault plane) is indicated by a dotted line.

magnitude M_w 1.9 seismic event occurred close to the network (Fig. 2) on 27 December 2007 (Yabe *et al.*, 2009). The mainshock was located about 30 m above the center of our network inside the dike. The event was followed by more than 25,000 aftershocks. From these about 11,500 events were located automatically. The aftershock sequence was monitored for five days. Most aftershocks clearly delineated the rupture plane (Yabe *et al.*, 2009), however, the mainshock also induced activity in ~80–140 m distance at the stope level. Because we limit our analysis on the Christmas vacation period of the mine, the aftershock sequence is not polluted by working noise or by postblasting activity. The majority of events occurred in direct proximity of the network, where location precision and detection threshold level are highest. Seismic events with frequencies exceeding 100 kHz were recorded in this area (Plenkers *et al.*, 2010). All picks and hypocenter locations used in this article were manually confirmed. The final aftershock dataset consisted of 9444 seismic events representing 82% of the automatically located aftershocks. Unfortunately, the acquisition system could not record the aftershock activity right after (~4.5 hrs) the occurrence of the mainshock due to overloading of the hard disc.

To investigate the frequency-magnitude characteristics of the recorded seismicity and potential variations of the magnitude of completeness with distance, we also selected several postblasting subsets from our catalog for a detailed analysis. These events occurred both before and after the M_w 1.9 event (Fig. 3a–c). The details of selected datasets are presented in Table 1. In Mponeng mine, blasting is performed on workdays at around 7 p.m., which is followed by a steep increase in seismic activity (Plenkers *et al.*, 2010). Subsequently, the seismic activity slowly decreases with time but is still clearly visible until the morning of the following day. Therefore, for each of the postblasting periods we chose the data between 7 p.m. and 6 a.m. of the following day. The day following blasts was always a holiday to reduce mining-induced noise. Similar to the aftershock dataset, the waveforms and onset picks were manually reviewed.

Spectral Analysis Using Acceleration Data

To combine information from accelerometer and AE sensors, we selected a subset of 135 strong seismic events from the aftershock sequence (Fig. 4). These events were extremely well recorded on both types of sensors, allowing us to compare the moment magnitude estimated from accelerometer with magnitudes estimated from AE sensors.

Spectral analysis was performed using the three-component accelerometer waveform data. The initial parts of the seismograms after *P* and *S* wave onset were used (window size = 1024 samples ≃2 ms; for stronger events, 2048 or 4096 samples were used). The selected waveforms were integrated twice in order to obtain ground displacement and smoothed using the von Hann's taper. The FFT transform was applied to calculate displacement spectra. The spectra were corrected for attenuation using the results of coda-Q analysis (Kwiatek *et al.*, 2009). The quality factor for shear waves varied between $Q_S = 200 - 600$ for frequencies ranging between 1 kHz and 17 kHz. For *P* waves, we assumed $Q_P = 5/2Q_S$. The spectra were not corrected for the transfer function of the accelerometer, as it is flat in the frequency band considered. The spectral levels Ω_C were picked manually from both *P* and *S* waves. The spectral levels were estimated for all three components of the accelerometer where possible; otherwise the calculated values were multiplied by an appropriate scaling factor. For the seismic moment, the following relation was used (i.e., Abercrombie, 1995):

$$M_0^C = 4\pi\rho c^3 R\sqrt{\Omega^2(X) + \Omega^2(Y) + \Omega^2(Z)}/F_c, \quad (1)$$

where ρ is the rocks' density (2900 kg/m^3), R is the source-receiver distance, and F_C is the mean radiation pattern (0.52 and 0.63 for *P* and *S* waves, respectively).

According to the locations of the events in the dike or the host rock, we used different wave velocities (Naoi *et al.*, 2008) estimated from transmission tests. Seismic moments for events that occurred within the dike were calculated using $V_P = 6.90 \pm 0.20$ km/sec, $V_S = 3.95 \pm 0.15$ km/sec. The values for the host rock were slightly lower: $V_P = 6.20 \pm 0.20$ km/sec, $V_S = 3.75 \pm 0.15$ km/sec. The seismic moment was averaged between seismic moments from *P* and *S* waves. The moment magnitude was calculated using the

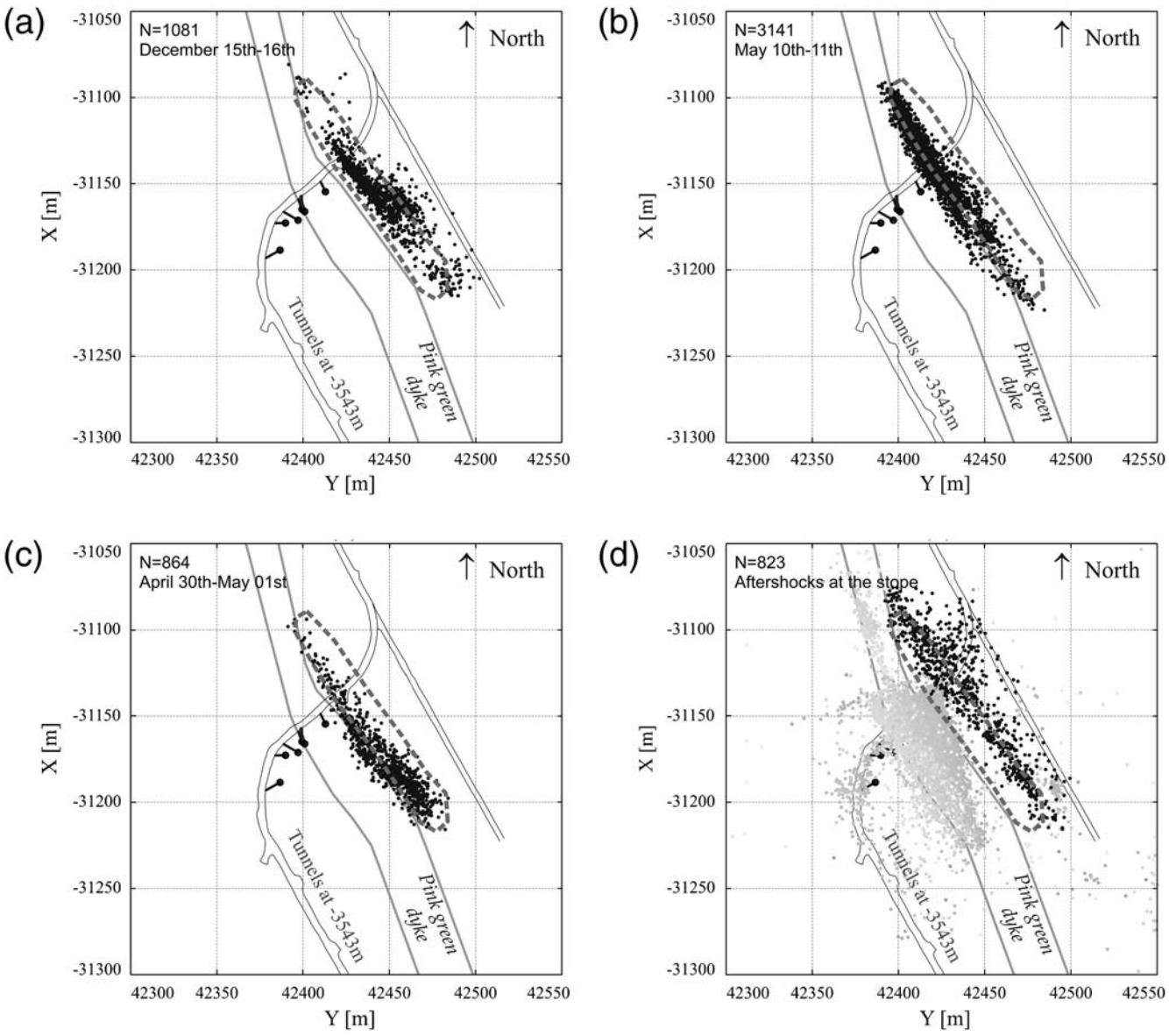

Figure 3. (a, b, c) The selected postblasting activity recorded during various periods of time. (d) The aftershock sequence at the stope level is shown together with remaining aftershock activity (gray dots) for comparison. The dashed line surrounds the area that is common to all datasets recorded at the stope level (see text for details). The approaching of the stope front to the dike is visible.

Table 1

Characteristics of the Zones Selected from Aftershock Sequence and Post-Blasting Datasets*

	Aftershock Sequence			Post-Blasting Activity			
	27 December 2007–2 January 2008			15–16 December 2007	10–11 May 2008	30 April –1 May 2008	Post-Blasting Activity Together
Zone	F	HF	S	S	S	S	S
N	7107	2591	823	1081	3057	841	4979
				Estimates Using Seismic Moment			
M_C	−4.30	−4.45	−3.00	−3.30	−3.40	−3.35	−3.40
$\hat{b}$	1.26	1.44	1.63	1.11 (1.16)	1.21 (1.19)	1.14 (1.15)	1.16 (1.17)
σ_b	0.02	0.03	0.08	0.04 (0.03)	0.02 (0.02)	0.05 (0.04)	0.02 (0.02)

*Zones: F, fault; HF, high-sensitivity; S, stope. N is the number of events; M_C is the magnitude of completeness; $\hat{b}$ is the estimator of the slope of GR relationship; and σ_b is the standard deviation of b value estimation. The values in parentheses represent parameters calculated for the area common to all datasets recorded at the stope level (cf. Fig. 3, see text for details).

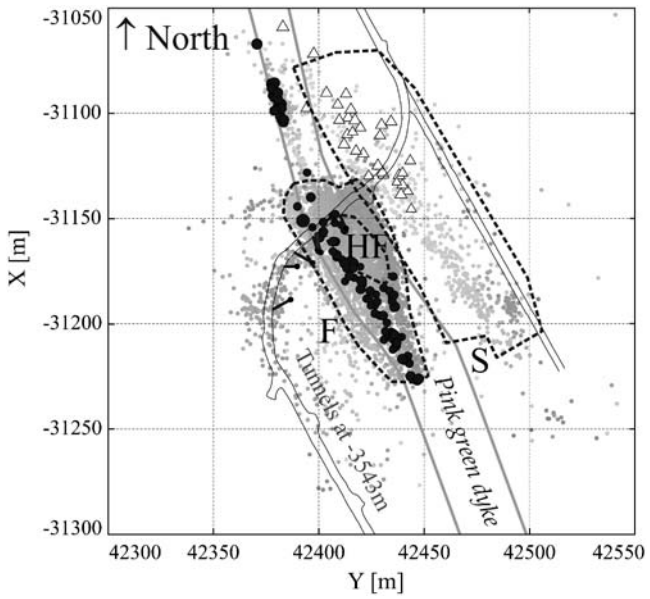

Figure 4. Spatial distribution of events selected for the spectral analysis (black points, white triangles for events in and outside the dike characterized by different wave velocities). The subdivision of the aftershock catalog into fault F, high-sensitivity (HF), and stope (S) zones is shown using dashed lines (see text for details). The events in zones F and S are clearly separated in depths, therefore they do not overlap.

standard relationship: $M_w\ 2/3 \log_{10} M_0 - 6.07$ (Hanks and Kanamori, 1979).

The moment magnitudes estimated from the three-component accelerometer recordings ranged from −4.1 to −0.3 with average uncertainties $<\pm 0.3$. To compare our results with other studies, we estimated corner frequencies and radiated energy using the calculated spectra, after correcting for a limited frequency band, as suggested by Ide and Beroza (2001). The relations between the corner frequency and seismic moment as well as radiated energy and seismic moment were investigated against other studies. The resulting estimates of static stress drop and apparent stress ranged from 1 MPa to 10 MPa and 0.05 MPa to 1 MPa, respectively. This is in good agreement with previous studies in a similar magnitude range (see, e.g., Gibowicz *et al.*, 1991; Jost *et al.*, 1998; Oye *et al.*, 2005). Our initial results show no deviation from the constant static stress-drop or from constant apparent stress models. A detailed analysis of the source scaling relations is a subject of the ongoing study.

Moment Magnitude Estimation from AE Sensors

The bandwidth of the three-component accelerometer is limited to a maximum frequency of 25 kHz. This does not allow us to record events with very low magnitudes <-4.2. Therefore, the AE sensors were used to investigate and extend the seismic catalog toward lower magnitudes. However, a different procedure for calculation of the moment magnitude was proposed. This is because the AE sensors were not calibrated in an absolute sense (i.e., the magnification factor was unknown). Moreover, the recorded amplitudes are affected by the *in situ* coupling quality of the sensor to the rock surface. The proposed method is not affected by these shortcomings and allows us to estimate the moment magnitude only from AE sensors.

For the analysis only five AE sensors were used. Signal quality of the remaining three sensors varied with time due to the insufficient coupling in the boreholes. High-pass filtering (750 Hz) was applied to the input waveforms. Subsequently, a 1024-sample length window following the P wave onset was selected. The signal-to-noise ratio (SNR) was estimated for each waveform separately using the noise window directly before the P wave arrival. Events with a SNR ratio below 10 dB were rejected.

Apparent magnitudes from AE recordings were initially calculated using two independent approaches. First, we estimated the energy flux J_i^* (asterisks denote quantities estimated with AE sensors, relative to calibrated values measured with the accelerometer) for AE sensor i:

$$J_i^* = \frac{1}{\gamma_i} \int V^2(f) df, \tag{2}$$

where $V(f)$ is the Fourier transform. Spectra were corrected for frequency-dependent attenuation using the coda-Q analysis, as in the case of the accelerometer. An additional correction, γ_i, has been applied for the incidence angle to account for the directivity effect. The correction factor, which depends on incidence angle and the frequency of the signal, were provided by GMuG (see, e.g., Manthei *et al.*, 2001). In our case the correction factor varied between $\gamma = 0$ dB for incidence angles of 0° with regard to the sensor and $\gamma = -25$ dB for incidence angle of 180° for the side-view sensor. We used P waves for which the applied procedure produced more reliable results than for S waves. Radiated energyE_i^* was estimated using the relation

$$E_i^* = J_i^* R V_P, \tag{3}$$

where the energy flux J_i^* was multiplied by the distance R and P wave velocity V_P.

Second, the apparent seismic moment was estimated using the following relation:

$$M_{0_i}^* = [2(K_i^{*3}/J_i^*)^{0.25}] R V_P^3, \tag{4}$$

where the quantity surrounded by square brackets is a spectral level (cf. Andrews, 1986) and K_i^* is the cumulated displacement waveform $D(f)$ squared (Snoke, 1987) and corrected for attenuation in a similar way as $V(f)$:

$$K_i^* = \frac{1}{\gamma_i} \int D^2(f) df. \tag{5}$$

We compared values of apparent radiated energy (E_i^*) and seismic moment ($M_{0_i}^*$) from AE sensors with moment magnitude (M_w) from the three-component accelerometer using selected seismic events as described previously. A linear regression analysis was performed to cross-calibrate

AE-derived $M_{0_i}^*$ or E_i^* estimates and moment magnitudes M_w from accelerometer recordings. Both estimates scaled with M_w estimated from the accelerometer. An example of cross-calibration for AE sensor 8 is shown in Figure 5. We measured the dispersion of points around the regression line. We found the dispersion is higher when E_i^* is used instead of seismic moment $M_{0_i}^*$. This is because E_i^* is more strongly controlled by attenuation than $M_{0_i}^*$. The uncertainties $\delta_i(\cdot)$ of the evaluation of $\hat{M}_w(\cdot)$ value for the AE sensor i were $\delta_i(E_i^*) < 0.70$, $\delta_i(M_{0_i}^*) < 46$. Therefore, we decided to use equation (4) as a measure of moment magnitude because it is expected to give smaller overall uncertainties to $\hat{M}_w(\cdot)$ estimation.

For any event from selected catalogs, we could estimate the moment magnitude for a specific event by means of the linear transformation of $M_{0_i}^*$ from all AE sensors available:

$$\hat{M}_w(M_0^*) = \frac{1}{N}\sum_{i=1}^{N} c_i \log(M_{0_i}^*) + d_i, \tag{6}$$

where c_i and d_i are the calculated regression coefficients for AE sensor i and N is the number of sensors used (maximum 5). The uncertainties of $\hat{M}_w(M_0^*)$ were calculated accounting for error propagation:

$$\delta(\hat{M}_w(M_0^*)) = \frac{1}{N_{\text{sensors}}}\sqrt{\sum_i \delta_i^2(M_0^*)}, \tag{7}$$

where $\delta_i(M_0^*)$is the uncertainty in prediction of the moment magnitude for AE sensor i. For $>64\%$ of events, moment magnitudes were calculated using five sensors. The uncertainties of $\hat{M}_w(M_0^*)$ do not exceed ± 0.46 (Table 1).

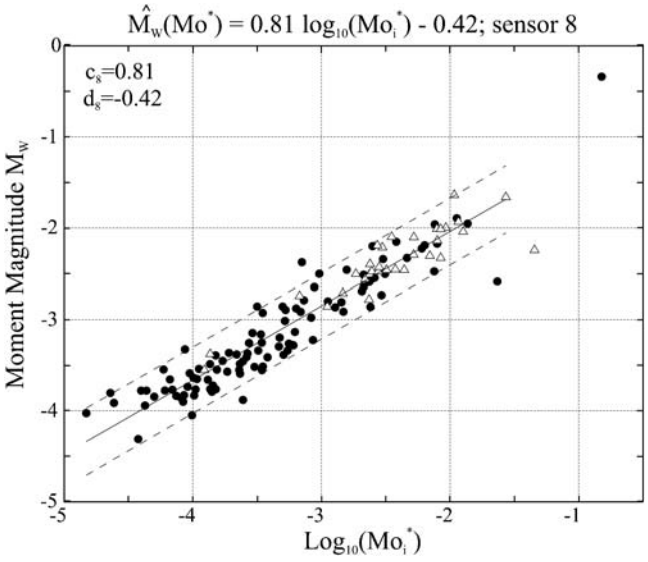

Figure 5. The relation of moment magnitude (M_w) calculated with the three-component accelerometer and logarithm of seismic moment M_0^* estimated for AE sensor 8. The dashed line represents the 95% confidence interval for prediction of a single $\hat{M}_w(M_0^*)$ value (see text for details). The different symbols reflect locations of selected events (cf. Fig. 4). The regression coefficients are shown in the top left part of the window.

Catalog Processing

The aftershock activity of the M_w 1.9 event was divided spatially into three zones (Fig. 4) to compare frequency-magnitude distributions and network detection thresholds. Zone F covers aftershock activity across the fault plane (Fig. 4, $N = 7107$ events). Zone S shows aftershock activity close to the stope level, reflecting the response of the stope front to the mainshock ($N = 823$ events). The frequency-magnitude characteristics of aftershock seismicity in this zone is compared to the postblasting activity around the stope. Finally, the third zone, HF, contains events from the zone of highest network sensitivity ($N = 2591$). There, extremely high-frequency events were recorded (Plenkers *et al.*, 2010). This zone shows the best sensor coverage and is best suited to investigate the lower limit of magnitude of completeness in our dataset.

Postblasting events were only observed in zone S, close to the stope level (Fig. 3a–c). We selected three time intervals with postblasting activity. The interval covers a time period before ($N = 1081$ events, Fig. 3a) and two periods after ($N = 3057$, $N = 851$, Fig. 3b,c) the M_w 1.9 event (see Table 1 for details).

For each selected zone, the magnitude of completeness, M_C, was estimated following the method proposed by Wiemer and Wyss (2000). We defined M_C value as the point where the power law fit 90% or more of the GR distribution. The slopes b of the GR relationship were estimated for each subset by means of the maximum likelihood formula (e.g., Utsu, 1965; see also Wiemer and Wyss, 2000 for details) using the M_C cutoffs calculated earlier:

$$\hat{\beta} = \frac{1}{\langle M_w(\cdot)\rangle - M_w^{\min}(\cdot)}, \tag{8}$$

where $\hat{\beta} = \hat{b}\ln(10)$, $\langle M_w(\cdot)\rangle$, and $M_w^{\min}(\cdot)$ are the mean and minimum magnitude in the analyzed subset. The corresponding standard deviation of b value estimates can be written as

$$\sigma_b = \frac{\hat{\beta}}{\ln(10)\sqrt{N}}. \tag{9}$$

We observe a trade-off between the assumed goodness of fit level (90%) and calculated M_C and b values. As a consequence, the b value is governed mainly by the GR distribution in the lowest magnitude range and therefore may be slightly underestimated.

Discussion and Conclusions

Richardson and Jordan (2002) found a bimodal GR relationship for data recorded in South African mines (that included data from Mponeng mine). The authors observed a rapid change in b value from a very steep to $b = \sim 1.0$ at $M_w \sim 0$. They attributed this change in b value to two fundamentally different types of seismic events: (1) type A: seismic events represent fracture dominated ruptures in intact rocks likely related to blasting and rockbursts and clustered in

time and space, and (2) type B: friction dominated ruptures on preexisting zones of weakness that represent tectonic earthquakes. According to their analysis, type B events (i.e., earthquakes) show a lower magnitude cut-off at $M_w \sim 0$. Recently, Boettcher *et al.* (2009) analyzed data recorded by the Tau-Tona mine seismic network, which is located nearby Mponeng mine investigated here. The authors observed no break down of the GR relation to a completeness level of $M_w - 1.3$.

The question arises whether the self-similar behavior of the GR relation can be extended to even lower magnitudes using our dataset. Figure 6 shows the cumulative GR relation for subsets of the data. Figure 6a,b shows the comparison between subsets from the aftershock sequence and postblasting activity, respectively. The detailed parameters of the subsets are presented in Table 1.

We found that the high-frequency aftershock data follow the Gutenberg–Richter relation with $\hat{b} = 1.26$ between $\hat{M}_w(M_0^*) - 4.4$ and -1.9. The events from the postblasting periods also seem to follow a GR relation with $\hat{M}_w(M_0^*)$ between -3.5 and -1.5 and a b value varying between $\hat{b} = 1.1$ and 1.21. Although the postblasting datasets display some disturbances for $\hat{M}_w(M_0^*) > -2.3$, this can be attributed to two technical factors described in the following paragraphs.

We observed the smallest M_C in zone HF ($M_C - 4.45$), that is, where sensor coverage is best and source-receiver distance < 45 m. The value for the zone F, across the fault plane, is only slightly higher ($M_C - 4.3$) because of higher source-receiver distances, frequently exceeding 60 m. In these areas, the majority of events occurred within the dike, characterized by low attenuation and reduced scattering of the seismic waves. Therefore, events with extremely low magnitudes could be detected from much further distances than from outside of the dike. It is striking that events with $\hat{M}_w(M_0^*) < -4.0$ and source radii of a few centimeters may be recorded from tens of meters away from the sensors. Events of that small size have so far only been observed in laboratory fracture studies (e.g., Davidsen *et al.*, 2007; Thompson *et al.*, 2009) or in controlled experiments that involved recordings of microcracking due to tunnel sealing (Collins *et al.*, 2002). The small magnitude events from our catalog overlap with events observed in laboratory tests performed on decimeter-sized rock samples. Our near-source observations suggest that with regard to statistical parameters such as b value, there is no evidence for a physical lower limit for the nucleation zone and minimum magnitudes down to $M_C - 4.4$.

The postblasting subsets display much higher completeness level ($M_C - 3.30$ to -3.40, $M_C - 3.40$ when postblasting data are combined together). This is related to longer source-receiver distances (median distance ~35 and ~100 meters for the fault and stope zones, respectively). In addition, waves travel through the dike/host rock contact and traverse severely damaged rock in the vicinity of the stope front.

The observed changes in the GR slopes for $\hat{M}_w(M_0^*) > -2.3$ are emphasized by two factors. First, the magnitudes of the strongest events are more likely to be underestimated because of the high-pass filter applied to the AE waveforms. This effect was unavoidable, as the AE recordings displayed a very unstable behavior at low frequencies. Second, we found GR distributions influenced by variations in spatial distribution of seismicity. For the postblasting activity we actually observe slightly different scenarios of GR behavior in a high-magnitude range (Fig. 6b). The GR of the postblasting activity before M_w 1.9 event (15–16 December 2007) displays the self-similar behavior up to magnitude -1.2. Although the remaining two postblasting subsets also display self-similar behavior, we observe a more or less stronger depletion in the number of high-magnitude events in comparison with the 15–16 December 2007 activity. Therefore, we

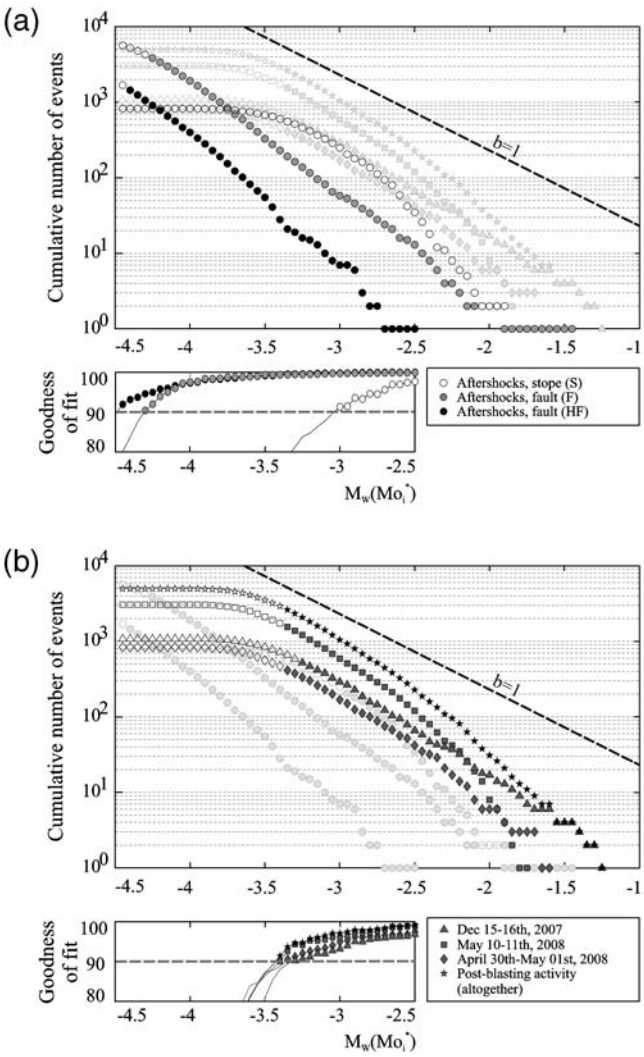

Figure 6. The cumulative Gutenberg–Richter relationships for selected data subsets (see Table 1 for details): (a) Subsets of aftershock activity constrained to fault (black dots), high-sensitivity (gray dots), and stope (white dots) zones; (b) postblasting activities (gray dots) at the stope level (cf. Fig. 3) and their combined distribution (black stars). The filled points show the part of the GR relationships over the magnitude of completeness, estimated using the method of Wiemer and Wyss (2000). The dashed line shows the slope assuming $b = 1$.

recalculated the GR relationships using the limited area that is common to all postblasting datasets and aftershocks recorded around the stope (dashed rectangles in Fig. 3). As a result, we found all postblasting datasets display much more homogeneous behavior with self-similar behavior of all subsets up to the moment magnitude −1.5 with b values in a range $\hat{b} = 1.16$–1.19 (for combined postblasting activity $\hat{b} = 1.17$). The roll-off of GR observed in a single dataset may be explained by a combined effect of spatial distribution of events and high-pass filter.

We observed no change in the magnitude-frequency distribution of events in a magnitude range between −4.4 and −1.9 for the aftershock dataset recorded on the fault plane, as well as for the postblasting datasets within a magnitude range −3.5 and −1.5.

In our study, the b values of the combined postblasting subset are lower than observed for type A seismicity below $M < 0$ (Richardson and Jordan, 2002; cf. fig. 3 therein); unfortunately, both datasets practically do not overlap. Richardson and Jordan (2002) considered type A seismicity as a response to blasting. In our postblasting data, the calculated b value follows rather the type B seismicity ($b = \sim 1.0$ reported by Richardson and Jordan, 2002 and $b = 0.76$–0.90 reported by Boettcher *et al.*, 2009). Our results suggest that there is no difference in frequency-magnitude relationships between postblasting data and regular (type B according to Richardson and Jordan, 2002) mining-induced seismicity. Therefore, the lower magnitude limit of the self-similarity in the GR relation may be extended down to at least −3.5. It is clear, however, that a more detailed comparison between Richardson and Jordan (2002), Boettcher *et al.* (2009), and our study requires selection of a common, carefully selected dataset, as we found b and M_C values sensitive to spatial and temporal selection of events (cf. differences in GR distributions for postblasting activity), even within the small exploitation area considered in our study. To investigate possible differences in the mechanisms of the rupture process, a detailed study of the source properties of recorded seismicity is required, as already suggested by Richardson and Jordan (2002).

We observe that the aftershock onfault activity in zone F is characterized by a higher value of b ($\hat{b} = 1.26$, standard deviation of b value $\sigma_b = 0.02$, see Table 1) than the postblasting activity at the stope level S for all analyzed periods. An even higher difference is visible when zone HF ($\hat{b} = 1.44$, $\sigma_b = 0.03$) and postblasting activities are compared. This is in agreement with behavior of aftershock sequences, which often show high b values in comparison with background activity. The difference in b value between the postblasting activity and aftershocks on the fault plane holds for a variety of reasonable values of the goodness of fit level (85%–95%). Our results are also in agreement with those of Ogasawara *et al.*, 2002, who analyzed the catalog before and after an M_w 2.0 event recorded in the Mponeng mine. They reported $b = 1.2$ for the aftershock sequence and $b = 1.0$ for the whole dataset ($N = 297$ events with $M_C > -1.7$).

Finally, an interesting feature comes from comparison between the postblasting activities and aftershock activity around the stope. For seismicity induced by blasting, we observe a higher proportion of high-magnitude events in comparison with the aftershocks induced naturally by M_w 1.9 event. This relation still holds even when we constrain all datasets to the same area. The origin of this difference is not very clear. One possible explanation is the overload of the acquisition system during the first hours of recording of the aftershock activity, when the system was recording more then 2000 events per hour and some (stronger) events from the stope level could be omitted/misspicked/not located because their waveforms frequently overlapped with intensive and distinct high-frequency activity from closer distances.

Summary

In this article, we present two distinct datasets recorded by a high-frequency seismic network sensitive in a frequency range 700 Hz–200 kHz using the three-component accelerometer and acoustic emission sensors. We investigate the magnitude of completeness and scaling issues of the aftershock activity of the M_w 1.9 event that occurred ~30 m from our network and the postblasting activity at the exploitation level located nearby (>~80 m). We found the level of completeness equal to approximately −4.4 and −3.5 for the aftershock sequence and postblasting activity, respectively. Both datasets can be described using GR power law. We do not observe the break down in a self-similarity in a moment magnitude range −4.4 to −1.9 for the aftershocks and −3.5 to −1.5 for the combined postblasting dataset. We found the b values of the aftershock sequence to be slightly higher ($\hat{b} = 1.26$) than for the postblasting activity at the stope level ($\hat{b} = 1.17$). We speculate postblasting datasets follow the type B seismicity, as reported by Richardson and Jordan (2002).

Data and Resources

Seismograms used in this article were collected using the JAGUARS (Japanese–German Underground Acoustic Emission and Microseismicity Research in South Africa) seismic network in the Mponeng gold mine. JAGUARS is a joint project of the University of Tokyo, Tohoku University, Ritsumeikan University (Japan), GFZ German Research Center for Geosciences, GMuG Gesellschaft für Materialprüfung und Geophysik (Germany), Seismogen CC, AngloGoldAshanti Ltd., ISS International, CSIR Johannesburg (South Africa). Data are currently not released to the public.

Acknowledgments

The authors want to thank T. H. Jordan, J. Davidsen, A. Cichowicz, and the anonymous reviewer for valuable remarks and comments. The Rock Engineering and Geology departments (R. Carstens, C. Miller, M. Pienaar, and G. Flitton) at the Mponeng gold mine (AngloGold Ashanti), ISSI in

Carletonville, and CSIR Johannesburg are acknowledged for providing us with useful information and many electronic materials. We would like to thank R. Barth and L. Vasquez for helping us with the manual preparation of the dataset. This article was partly supported by Grant-in-Aid for Scientific Research (A-18253003), Earthquake Research Institute cooperative research program, Tohoku University's 21st Century COE program, and Observation and Research Program for Prediction of Earthquakes and Volcanic Eruptions of the Ministry of Education, Culture, Sports, Science, and Technology (MEXT) of Japan.

References

Abercrombie, R. (1995). Earthquake source scaling relationships from $M_L - 1$ to 5 using seismograms recorded at 2.5-km depth, *J. Geophys. Res.* **100,** 24015–24036.

Aki, K. (1987). Magnitude frequency relation for small earthquakes: A clue to the origin of fmax of large earthquakes, *J. Geophys. Res.* **92,** 1349–1355.

Andrews, D. (1986). Objective determination of source parameters and similarity of earthquakes of different size, in Das, S., J. Boatwright, and C. Scholz (Editors), *Earthquake Source Mechanics* **37,** 259–267.

Boettcher, M. S., A. McGarr, and M. Johnston (2009). Extension of Gutenberg–Richter distribution to $M_w - 1.3$, no lower limit in sight, *Geophys. Res. Lett.* **36,** L10307, doi 10.1029/2009GL038080.

Brace, W. F., and J. D. Byerlee (1966). Stick-slip as a mechanism for earthquakes, *Science* **153,** no. 3739, 990–992.

Collins, D. S., W. S. Pettitt, and R. P. Young (2002). High-resolution mechanics of a microearthquake sequence, *Pure Appl. Geophys.* **159,** 197–219.

Davidsen, J., S. Stanchits, and G. Dresen (2007). Scaling and universality of rock fracture, *Phys. Rev. Lett.* **98,** 125502.

Dieterich, J. H. (1979). Modeling of rock friction, 1: experimental results and constitutive equations, *J. Geophys. Res.* **84,** 2161–2168.

Dieterich, J. H. (1992). Earthquake nucleation on faults with rate- and state-dependent strength, *Tectonophysics* **211,** 115–134.

Gibowicz, S. J., R. P. Young, S. Talebi, and D. J. Rawlence (1991). Source parameters of seismic events at the Underground Research Laboratory in Manitoba, Canada: Scaling relations for events with moment magnitude smaller than 2, *Bull. Seismol. Soc. Am.* **81,** 1157–1182.

Hanks, T. C., and H. Kanamori (1979). A moment magnitude scale, *J. Geophys. Res.* **84,** 2348–2350.

Ida, Y. (1973). The maximum acceleration of seismic ground motion, *Bull. Seismol. Soc. Am.* **63,** 959–968.

Ide, S., and G. C. Beroza (2001). Does apparent stress vary with earthquake size?, *Geophys. Res. Lett.* **28,** no. 17, 3349–3352.

Jost, M. L., T. Busselberg, O. Jost, and H.-P. Harjes (1998). Source parameters of injection-induced microearthquakes at the KTB deep drilling site, Germany, *Bull. Seismol. Soc. Am.* **88,** 815–832.

Kanamori, H., and T. H. Heaton (2000). Microscopic and macroscopic physics of earthquakes, *Geocomplexity and the Physics of Earthquakes*, D. T. J. Rundle and W. Klein (Editors), 147–183.

Kwiatek, G., K. Plenkers, and M. Naoi (2009). Mining-Induced Seismicity recorded by a high-frequency seismic network (100 Hz to 170,000 Hz) in a Deep Gold Mine in South Africa (JAGUARS project): Attenuation and scattering effects, *Proceedings of the 69. Jahrestagung der Deutschen Geophysikalischen Gesellschaft*, Christian-Albrechts-Universität zu Kiel, Kiel, Germany, 23–26 March, 2009.

Manthei, G. (2005). Characterization of acoustic emission sources in a rock salt specimen under triaxial compression, *Bull. Seismol. Soc. Am.* **95,** 1674–1700.

Manthei, G., J. Eisenblätter, T. Spies, and G. Eilers (2001). Source parameters of acoustic emission events in salt rock, *J. Acoustic Emission* **19,** 100–108.

McGarr, A. (1999). On relating apparent stress to the stress causing earthquake fault slip, *J. Geophys. Res.* **104,** 3003–3011.

Nakatani, M., Y. Yabe, J. Philipp, G. Morema, S. Stanchits, and G. Dresen-JAGUARS-Group (2008). Acoustic Emission Measurements in a Deep Gold Mine in South Africa—Project Overview and Some Typical Waveforms, *Seis. Res. Lett.* **79,** no. 2, 311.

Naoi, M., M. Natakani, Y. Yabe, and J. Philipp (2008). Very high frequency AE (<200 kHz) and microseismicity observation in a deep South African gold mine—Evaluation of the acoustic properties of the site by the in-situ transmission test, *Proceedings of the 2008 SSA Annual Meeting*, 16–18 April 2008, Santa Fe, New Mexico.

Ogasawara, H., S. Sato, S. Nishii, H. Kawakata, and The research group for semi-controlled earthquake generation experiments in South African deep gold mines (2002). Temporal variation of seismic parameters associated with an $M_w \sim 2$ event monitored at a $100 \sim 200$ m distance, *Seismogenic Process Monitoring* H. Ogasawara, T. Yanagidani, and M. Ando (Editors), Balkema, Rotterdam.

Oye, V., H. Bungum, and M. Roth (2005). Source parameters and scaling relations for mining-related seismicity within the Pyhäsalmi ore mine, Finland, *Bull. Seismol. Soc. Am.* **95,** 1011–1026.

Plenkers, K., Kwiatek, G. Dresen, and JAGUARS-Group (2010). Observation of seismic events with frequencies $f > 25$ kHz at Mponeng deep gold mine, *Seism. Res. Lett.* (in press).

Rice, J. R., and M. Cocco (2007). Seismic fault rheology and earthquake dynamics in tectonic faults: Agents of change on a dynamic Earth, M. R. Handy, G. Hirth, and N. Hovius (Editors), pp. 99–137, The MIT Press, Cambridge, Massachusetts.

Richardson, E., and T. Jordan (2002). Seismicity in deep gold mines of South Africa: Implications for tectonic earthquakes, *Bull. Seismol. Soc. Am.* **92,** 1766–1782.

Snoke, J. A. (1987). Stable determination of (Brune) stress drop, *Bull. Seismol. Soc. Am.* **77,** 530–538.

Thompson, B. D., R. P. Young, and D. A. Lockner (2009). Premonitory acoustic emissions and stick-slip in natural and smooth-faulted Westerly granite, *J. Geophys. Res.* **114,** B02205.

Utsu, T. (1965). A method for determining the value of b on the formula $\log n = a - bM$ showing the magnitude-frequency relation for earthquakes, *Geophys. Bull.* Hokkaido Univ. **13,** 99–103.

Wiemer, S., and M. Wyss (2000). Minimum magnitude of completeness in earthquake catalogs: Examples from Alaska , the Western United States, and Japan, *Bull. Seismol. Soc. Am.* **90,** 859–869.

Yabe, Y., J. Philipp, M. Nakatani, G. Morema, M. Naoi, H. Kawakata, T. Igarashi, G. Dresen, and H. OgasawaraJAGUARS (2009). Observation of numerous aftershocks of an M_w 1.9 earthquake with an AE network installed in a deep gold mine in South Africa. *Earth Planets Space* **61,** e49–e52.

Helmholtz Centre Potsdam
GFZ German Research Centre for Geosciences
Telegrafenberg, 14473
Potsdam, Germany
kwiatek@gfz-potsdam.de
katrinp@gfz-potsdam.de
dre@gfz-potsdam.de
(G.K., K.P., G.D., JAG-Grp.)

Earthquake Research Institute of the University of Tokyo
Tokyo, 113-0032, Japan
nakatani@eri.u-tokyo.ac.jp
(M.N.)

Tohoku University
Sendai, Miyagi 980-8578, Japan
yabe@aob.geophys.tohoku.ac.jp
(Y.Y.)

Manuscript received 4 September 2009